Journal of Power Sources 659 (2025) 238403

Contents lists available at ScienceDirect

Journal of Power Sources

journal homepage: www.elsevier.com/locate/jpowsour

The induced linkage mechanism in three-dimensional electrolyte architecture to promote ion transport of solid-state Li-S batteries

Hongxu Zhou [a], Yiyang Zhao [a], Xiaoning Wang [a], Jingang Zheng [a], Weichen Han [a], Hongwei Zhao [a], Han Zhang [a], Lixiang Li [a], Xin Geng [a], Baigang An [a], Chengguo Sun [a,b,*]

[a] School of Chemical Engineering University of Science and Technology Liaoning, Anshan, 114051, China
[b] School of Chemical Engineering Nanjing University of Science and Technology, Nanjing, 210094, China

HIGHLIGHTS

- 3D cathode and solid-polymer electrolyte were designed by integrated strategy.
- Induced linkage mechanism effectively mitigates the polysulfide shuttle effect.
- The capacity decay rate of the battery is only 0.052 % after 500 cycles at 1 C.

GRAPHICAL ABSTRACT

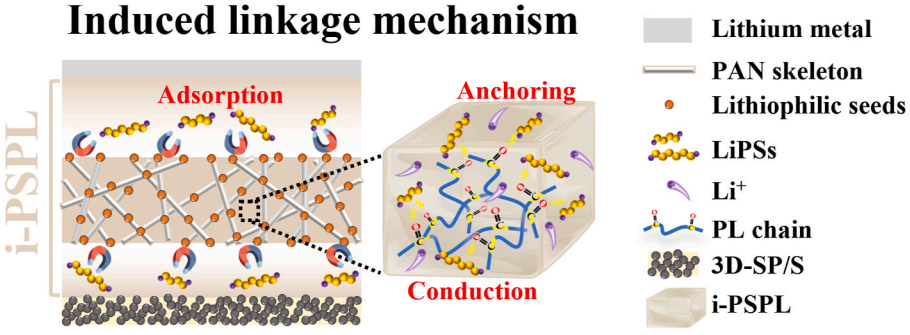

ARTICLE INFO

Keywords:
Ion transport kinetics
Induced linkage mechanism
Polysulfides shuttling
Integrated electrolyte
Solid-state Li-S batteries

ABSTRACT

Severe interfacial issues, sluggish ion transport kinetics, and polysulfides shuttling are consistently considered major barriers to hinder the high-performance solid-state lithium-sulfur (Li-S) batteries. Herein, an integrated design based on induced linkage mechanism is adopted to fabricate the high-performance Li-S batteries by combining three-dimensional (3D) cathode and 3D solid electrolyte. The 3D solid electrolyte architecture consists of cyclized polyacrylonitrile (PAN) fiber skeleton embedded with SiO_2, and is filled with in-situ polymerized pentaerythritol tetraacrylate (PETEA) containing appropriate liquid electrolyte (PL). SiO_2 particles priorly attract lithium polysulfides (LiPSs) to the 3D electrolyte skeleton due to high affinity for LiPSs, inducing the linkage mechanism to proceed. Then the C=O groups of the polymerized PL can anchor LiPSs within the 3D solid electrolyte, which can further serve as a rapid ion transport medium to ensure efficient ion transfer. Furthermore, the carbon skeleton of 3D cathode provides a reversible transport channel for LiPSs and sufficient permeation space for PL. The smooth "adsorption-anchor" linkage conduction process shows outstanding ionic conductivity (7.34×10^{-3} S cm^{-1}, 25 °C). The assembled solid-state Li-S batteries exhibit excellent cycling stability with a capacity decay rate of 0.052 % (500 cycles, 1 C). The pouch cells also demonstrate stable reversible capacity and outstanding safety performance.

* Corresponding author. School of Chemical Engineering University of Science and Technology Liaoning, Anshan, 114051, China.
E-mail address: sunyangguo2004@163.com (C. Sun).

https://doi.org/10.1016/j.jpowsour.2025.238403
Received 6 January 2025; Received in revised form 2 September 2025; Accepted 13 September 2025
Available online 20 September 2025

1. Introduction

Solid-state lithium-sulfur (Li-S) batteries have emerged as the most promising candidates for their huge advantages of ultra-high energy density (2600 Wh kg^{-1}), low cost, and non-toxicity to the environment [1–3]. More importantly, both non-flammable and non-volatile properties of the solid-state electrolytes (SSEs) also provide a high level of safety over conventional liquid electrolytes (LEs) [4,5]. However, the poor interface contacts between electrodes and electrolytes, and the SSEs with low room-temperature ionic conductivity will greatly deteriorate the electrochemical performance of Li-S batteries [6,7]. To address these issues, semi-solid polymer electrolytes (SSPEs) have been widely investigated due to their excellent flexibility and good interfacial contact with electrodes [8–10]. Although the liquid content in SSPEs is greatly reduced, they still maintain a high ionic conductivity over 10^{-3} S cm^{-1}.

Due to the presence of residual liquid in SSPEs, the shuttling effect of polysulfides still exists during cycling. Some effective strategies are adopted by modifying electrodes or electrolytes to mitigate the shuttling effect [11]. For cathodes, the most common approaches are to develop electrocatalysts adsorbed on carbon-based materials to anchor polysulfides via chemical adsorption [12]. A bilayer carbon matrix modified with Ni-doped CoSe2 nanoparticles has been developed, which effectively suppressed the shuttling effect, resulting in a capacity decay of only 0.07 % at 1 C [13]. Diatomaceous earth was added to the in-situ synthesis of DOL-GPE (PDOL-$SiCl_4$-DE), showing the strong affinity for polysulfides by absorption [4]. MnO_2-ZnS p-n heterojunction and spontaneous built-in electric field were combined to design a functional coated separator, in which MnO_2 nanowires provide suitable adsorption capacity for polysulfides, resulting in a capacity decay rate of merely 0.048 % per cycle [14]. B-doped Ni_2P catalyst can effectively control the shuttling of polysulfides, where the electron donation from B to P can further enhance the adsorption of polysulfides on catalysts, so the capacity decay rate at 2 C per cycle is only 0.024 % [15]. In other cases, some metal-metal compound composite materials are employed to catalyze the rapid conversion of polysulfides, which can reduce shuttling effect due to the high catalytic activity for polysulfides [16,17]. A three-dimensional (3D) cathode decorated with NiCo bimetallic particles exhibits high catalytic activity, accelerating reaction kinetics and mitigating shuttling effect [18]. The above-mentioned methods can effectively alleviate the problem of polysulfides shuttling. However, the low transference number (t_{Li}^{+}) at room temperature and the poor charge transport kinetics at the electrode/electrolyte interface are still major barriers to restrict performance of Li-S batteries [19]. Inspired by the transport properties of solid electrolytes, halide electrolytes have been applied in Li-S batteries to enhance macroscopic ionic conductivity [20]. In addition, Park et al. designed the flexible single-layer composite electrolyte PAES-g-PEG by dispersing Li_6PS_5Br nanoparticles into organic matrix, which can not only improve the ionic conductivity through extending ion conducting cluster dimension, but also increase the mechanical strength of the composite electrolyte [21]. All of these results have made remarkable progress for solving problems of Li-S batteries. However, individual strategy makes it difficult to optimize the overall performance of the battery [22]. It is necessary to develop an integrated technology to achieve rapid Li^+ transport and alleviate the lithium polysulfides (LiPSs) shuttling during cycling.

Herein, we combine 3D cathode and solid-polymer electrolyte in an integrated design based on the induced linkage mechanism. The cathode employs 3D carbon skeleton prepared in our previous work as the sulfur host (denoted as 3D-SP/S) [23]. The abundant internal porous structure facilitates infiltration of polymer precursor solution, enhances electrode-electrolyte interface compatibility, and provides reversible transport channels for LiPSs. Solid-polymer electrolyte (i-PSPL) consists of the cyclized 3D electrospun polyacrylonitrile (PAN) fiber skeleton with embedded SiO_2 (h-PSi), which is filled with in-situ polymerized pentaerythritol tetraacrylate (PETEA) containing appropriate liquid electrolyte (PL). Due to high affinity with LiPSs, SiO_2 particles priorly attract them on the h-PSi skeleton. Subsequently, the C=O functional groups in polymerized PL can rapidly anchor LiPSs to realize the "adsorption-anchoring" process. The i-PSPL electrolyte after anchoring LiPSs can exhibit excellent ion transport ability and be used as a fast ion transport medium. Therefore, the linkage mechanism induced by "adsorption-anchoring" of LiPSs improves the ionic conductivity within batteries and realizes linkage conduction process smoothly. Benefiting from the 3D electrode-electrolyte integrated design and induced linkage mechanism, the batteries exhibit excellent room temperature ionic conductivity (7.34×10^{-3} S cm^{-1}), ion migration capability (t_{Li+} = 0.47), and superior long cycling performance with a low-capacity decay of 0.052 % per cycle at 1 C after 500 cycles. Even at a high temperature of 60 °C and current density of 2 C, the cell also maintains a stable reversible discharge capacity of 586.2 mAh g^{-1} after 900 cycles. Furthermore, Li-S pouch cell also shows stable operation and superior safety under mechanical damage. The work offers a new design idea for solving the issues of shuttle effect and charge transfer problems in high-performance semi-solid-state Li-S batteries.

2. Result and discussion

The fabrication process of the "electrode-electrolyte" integrated design is shown in Fig. 1a. Firstly, SiO_2-loaded PAN nanofiber membrane (PSi) was prepared by electrospinning, after low-temperature heat treatment (210 °C), we can obtain the partially cyclized PAN membrane (h-PSi). The flexibility of h-PSi has been demonstrated to be excellent through the process of folding and unfolding (Fig. S1a). The specific cyclization process of PAN is shown in Fig. S1b, and the morphology and structure of the PSi, h-PSi membrane, and filled with in-situ polymerized PETEA containing appropriate liquid electrolyte (i-PSPL) were examined by scanning electron microscopy (SEM). As shown in Fig. 1b, the color of electrolyte membrane turns from white to pale yellow after heat treatment. The cyclized 3D PAN nanofibers with uniform distribution of SiO_2 were observed in Fig. 1c and S2a, a single fiber in the h-PSi membrane has a diameter of about 220 nm (Fig. S2b) and the membrane has a thickness of about 70 μm (Fig. 1d). Simultaneously, the morphology of i-PSPL electrolyte polymerized on h-PSi membrane with PETEA as monomer was also shown in Fig. 1e and f. The 3D pores in the h-PSi membrane were fully filled, and the above results were also confirmed by Fig. S3.

In order to evaluate the affinity of the h-PSi membrane to electrolyte, the contact angle, porosity, and electrolyte uptake rate were investigated. The non-polar structure of polypropylene separators (PP separator, Celgard 2500) exhibits hydrophobicity and poor compatibility with liquid electrolyte (LE, 1 M LiTFSI in DME:DOL = 1:1 with 2 wt% $LiNO_3$), which will significantly impact the rate performance and lifespan of the batteries [24]. As shown in Fig. 2a, the LE was dropped on h-PSi membrane, it can be found that liquid drop can rapidly penetrates along the pores, which is attributed to the interlaced nanofiber structure. In contrast to PP separator with parallel small holes (Fig. S4a), the h-PSi membrane exhibits a lower contact angle of 7.833°. Additionally, the diffusion capacity of the electrolyte is also an important indicator to examine battery performance, which can ensure that the precursor solution fully penetrated the battery in less time to effectively improve production efficiency [25]. Fig. 2b shows the diffusion capacity of LE on the PP separator and h-PSi membrane along the vertical direction. After soaking for 30 min, the height where the liquid rises along the h-PSi electrolyte membrane was twice that of PP separator. The results are good consistent with the calculation of high porosity (87 %) and electrolyte uptake rate (330 %) in Fig. S4b. Thermal stability is another critical parameter for high-power batteries, benchmarking against the safety of battery system. Fig. 2c presents the changes of shape of two electrolyte membranes after heating. Compared to PP membrane, the PSi remains flat without significant shrinkage at 120 °C. This result proves that the PSi membrane has outstanding thermal stability to

ensure the safe operation of the battery at higher temperatures.

The assembly of batteries and the polymerization mechanism of PL within h-PSi membrane are illustrated in Fig. 3a. The free radicals derived from the high-temperature decomposition of azobisisobutyronitrile (AIBN) can attack C=C bonds of PETEA monomer to generate active sites, thus triggering monomer polymerization. Due to the presence of a small amount of liquid, the polymerized PETEA can mix the solvent molecule to form milky white SSPE (Fig. S5). Fourier-transform infrared (FTIR) spectral analysis also confirmed the polymerization process. As shown in Fig. 3b, the typical peak of 1630 cm^{-1} corresponding to C=C bonds of PETEA disappeared after polymerization. Furthermore, the characteristic peak of the C ≡ N bond at 2253 cm^{-1} in the PSi membrane disappeared in the i-PSPL electrolyte, and a new peak formed at 1670 cm^{-1}, corresponding to C=N bond. This further confirms the successful cyclization of PAN. To evaluate the "adsorption-anchoring" ability of i-PSPL electrolyte for polysulfides. Fig. 3c demonstrates the permeation resistance of the PP separator and i-PSPL electrolyte to polysulfides. For PP separator, the Li_2S_6 can migrate from left to right across the separator, and after 24 h, the solution on the right turned dark yellow. In contrast, only little brown-yellow polysulfides diffused through i-PSPL to the right, exhibiting that it has a significant superiority in polysulfides blocking effect.

To further explore the reason for the inhibition of polysulfides shuttling by i-PSPL electrolyte, FTIR spectra of PETEA and the i-PSPL electrolyte after 200 cycles are presented in Fig. 4a. It can be clearly seen that the peak corresponding to the carbonyl group (C=O) in PETEA at 1717 cm^{-1} disappears in i-PSPL electrolyte after cycling, indicating that polysulfides have been absorbed on the ester functional groups, while the peak position of -CH_2 near the ester group has also shifted from 1407 and 1473 cm^{-1} to 1422 and 1489 cm^{-1} due to the change of chemical environment. The above results were also confirmed by X-ray photoelectron spectroscopy (XPS) spectra of i-PSPL electrolyte before and after cycling. The O 1s spectrum of the i-PSPL electrolyte before cycling shows three peaks at 533.01 eV, 531.94 eV, and 530.65 eV assigned to Si-O, C-O-C, and C=O, respectively. After 200 cycles, the peak of C=O virtually disappears (Fig. S6a). Further evidence can be confirmed by C 1s spectrum; the disappearance of C=O peak at 289.1 eV after cycling (Fig. S6b) proves the anchoring effect of C=O on LiPSs [26,27]. The mechanism of i-PSPL absorbed polysulfides electrolyte has been demonstrated through density functional theory (DFT) calculations, clarifying the significance of the chemical adsorption of polysulfides by C=O bond in PETEA. Fig. S7 shows the electrostatic potential distribution maps in the stable configurations for PETEA, Li_2S_8, Li_2S_6, PP, and PAN, which can be used to describe the coordination situation between polysulfides and polymers. Because PETEA is a perfectly symmetric star structure, one basic unit is used to calculate the binding energy (Fig. S8). As shown in Fig. 4b and S9, PETEA has the highest binding energy of −0.85 eV and −0.81 eV with Li_2S_8 and Li_2S_6, respectively, which is almost 14–27 times higher than that of PP monomer. Fig. 4c shows the in-situ optical microscopy of lithium dendrite growth during discharge process using i-PSPL electrolyte. It can be found a lot of lithium dendrites formation on the lithium metal surface in LE during a short period (25 min) due to irregularly deposit of Li^+. On the contrary, after cycling 2 h, no lithium dendrites were observed on the surface of lithium metal using i-PSPL electrolyte, which is attributed to the preferential induction deposition of Li^+ by uniform SiO_2 lithiophilic particles in i-PSPL [28]. It shows the phenomenon of dendrite-free growth, reflecting the high safety and inhibition of lithium dendrites in batteries. Based on the above experimental results, it can be inferred that the diffusion of polysulfides in i-PSPL should be as follows: The LiPSs are priorly adsorbed on the h-PSi skeleton due to SiO_2 particles high affinity, and then the C=O in the polymerized PL can anchor them to inhibit the diffusion of polysulfides. To visualize the process, a series of contrast experiments were designed to validate the accuracy of the aforementioned inferences (see Supplementary Video S1). SiO_2, PETEA, and the mixture of SiO_2 and PETEA (labeled as SiO_2-suspension) were separately added to Li_2S_6 solution to observe the color changes. The deep color of Li_2S_6 solution was used as a standard comparison sample. In contrast to the light color observed in SiO_2, the direct decolorization of the solution after PETEA addition indicates a strong anchoring effect of C=O groups in PETEA for polysulfides. However, the Li_2S_6 solution showed a process of fade followed by decolorization after dropping the SiO_2-suspension. In order to observe the results more clearly, the above solutions were left to stand for 5 min and 12 h, respectively. As shown in Fig. S10a–b, SiO_2-suspension-injected Li_2S_6 solution displayed phase separation, demonstrating that SiO_2 priorly adsorbed the polysulfides in the upper phase, forming a pale-yellow SiO_2 adsorption layer. The lower phase was PETEA anchoring layer, which was completely decolorized. After standing the phase-separated solution for 12 h, the delamination disappeared and the pale-yellow SiO_2 adsorption layer also completely decolorized. This indicates that the strong anchoring effect of C=O groups can anchor all the polysulfides adsorbed by SiO_2 (Fig. S10c). Therefore, the "adsorption-anchoring" linkage mechanism was realized in batteries. We regarded the

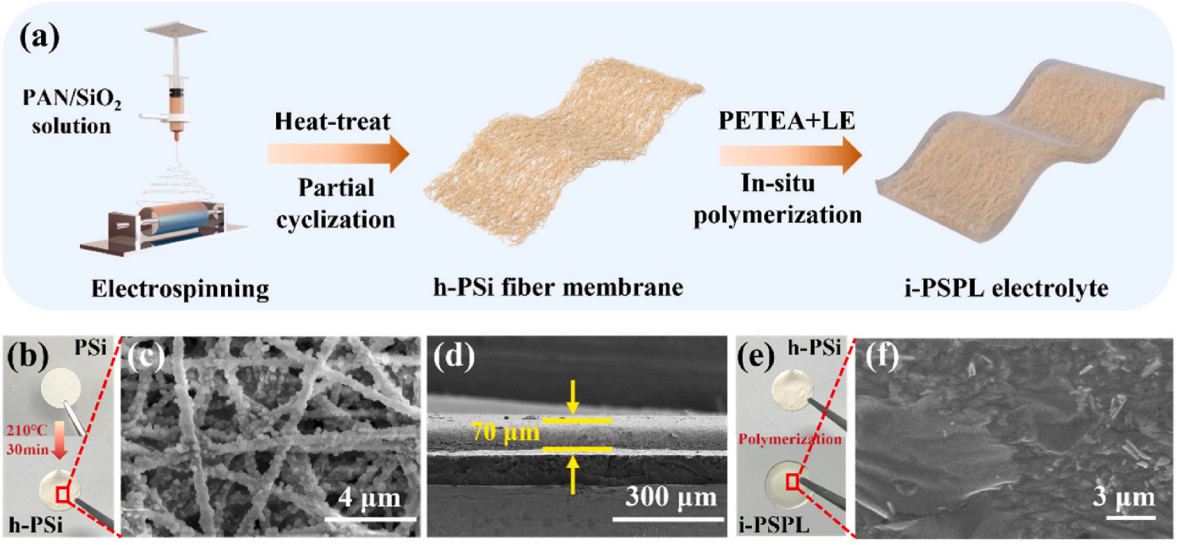

Fig. 1. (a) Schematic illustration of the fabrication process of i-PSPL solid-state electrolyte. (b) Digital picture of PSi and h-PSi membrane. (c) SEM image of h-PSi. (d) Cross-sectional SEM image of h-PSi membrane. (e) Digital picture of i-PSPL solid-state electrolyte after in-situ polymerization. (f) SEM image of i-PSPL.

"adsorption-anchoring" process as the SiO_2-induced linkage process, which is the origin of the induced linkage mechanism.

To evaluate the electrochemical stability of i-PSPL electrolyte, the electrochemical stability window was tested by linear sweep voltammetry (LSV). As shown in Fig. 5a, i-PSPL exhibits an electrochemical stability window of up to 4.8 V versus Li^+/Li, slightly higher than LE (4.7 V). The result demonstrates the excellent redox stability of i-PSPL electrolyte. Fig. 5b depicts the curves of the Li^+ transference number (t_{Li}^+) for i-PSPL and LE, the t_{Li}^+ of i-PSPL electrolyte is 0.47, which is much higher than LE (0.39). The strong electron-withdrawing capabilities of polar functional groups such as C=N, C-O-C, and C=O played a crucial role for Li^+ migration process [29]. To elucidate the contribution of h-PSi framework to the performance in i-PSPL, a similar solid electrolyte named i-PPPL was prepared by using PP separator instead of h-PSi. Fig. 5c displays the Nyquist plots of 3D-SP/S||i-PPPL||Li and 3D-SP/S||i-PSPL||Li, and both cells exhibit a semicircle in the high-frequency region and a sloped line in the low-frequency region. The fitted results reveal the 3D-SP/S||i-PSPL||Li cell presents a low charge transfer resistance (R_{ct}) of 89 Ω, which is about 3 times less than that of i-PPPL (Table S1). The result indicates that the h-PSi membrane as a scaffold for i-PSPL can provide continuous and fast ion channels, thereby improving the rapid migration of Li^+ to the cathode and reducing the resistance of ion transport. Furthermore, we also prepared i-PSPL electrolyte by the ex-situ polymerization method (Fig. S11). In comparison to in-situ polymerization method, an additional semicircle related to the ionic resistance of solid electrolyte (R_f) emerged in the high-frequency region. The data fitted by equivalent circuit diagram shows that the interface impedance of i-PSPL prepared by ex-situ is even 100 times higher than that of in-situ polymerization (Table S2). To demonstrate the interface stability of batteries by in-situ method, the 3D-SP/S||i-PSPL||Li asymmetric battery was assembled and placed for 20 days. As shown in Fig. S12, the interface resistance increases by about 50 Ω for 15 days, and keeps the same values with the prolonging of time, proving a stable interface formed between i-PSPL electrolyte and electrodes.

Fig. 5d shows the cyclic voltammetry (CV) curves with a voltage range at 1.7 V–2.8 V and 0.1 mV s^{-1}. For 3D-SP/S||i-PSPL||Li batteries, there is only a pair of redox peaks located at 2.6 V and 1.9 V in the curves, which are consistent with the characteristic peaks of solid-state Li-S system [22]. With the increase of the cycling numbers, CV curves are the same as the beginning, indicating that i-PSPL has good stability and stronger inhibition of polysulfides [30]. The Li^+ mobility in i-PPPL and i-PSPL was tested through galvanostatic intermittent titration technique (GITT) experiments (Fig. 5e and S13). In contrast to 3D-SP/S||i-PPPL||Li cell, batteries with i-PSPL have smaller internal resistance and higher ion diffusion coefficient, indicating fast reaction kinetics in Li-S batteries (Fig. S14). These outcomes are attributed to the integrated 3D electrode-electrolyte and induced linkage mechanism, where the i-PSPL electrolyte after anchoring polysulfides can act as a fast ion transport medium, facilitating efficient charge transfer, thereby enhancing reaction kinetics. The test results of ionic conductivity and activation energy for i-PSPL are 7.34×10^{-3} S cm^{-1} and 0.074 eV at room temperature (Fig. 5f–S15 and S16), which are comparable to LE (4.78×10^{-3} S cm^{-1}, 0.054 eV). The high activation energy of i-PSPL electrolyte is attributed to the hindered ion conduction in the high viscosity. The symmetric cell with i-PSPL was tested at a selected plating/stripping capacity of 0.5 mAh cm^{-2} (Fig. 5g), which delivered a low overpotential (145 mV) during 600 h, and the enlarged image of inset figures illustrate the stable cycling in symmetric battery. In contrast, the battery with LE only cycles for 302 h at 0.5 mAh cm^{-2} before short-circuit (Fig. S17). In addition, SEM images and digital photos of the cycling Li||Li symmetric batteries show that the lithium metal matching i-PSPL exhibits uniform deposition, while matching LE exhibits serious uneven deposition (Fig. S18). The above results correspond to the ability of uniform deposition of lithium, which is attributed to the lithiophilic seeds (SiO_2) in i-PSPL electrolyte. Since Li nucleation and deposition preferentially occur on the surface of polar metal oxides, the introduction of SiO_2 provides an advantage for uniform deposition of Li [31]. This also reflects the positive effect of the induced linkage mechanism for ion transport inside the batteries.

Electrochemical assessments were carried out to investigate the performance of i-PSPL electrolyte in Li-S batteries. Fig. 6a shows that i-PSPL electrolyte achieves polysulfides confinement and uniform Li deposition on the anode surface through the fast ion channels formed by the induced linkage mechanism. Fig. 6b corresponds to the charge and discharge curves at different current densities from 0.05 C to 5 C. The platform shown in the discharge curves also corresponds to a pair of

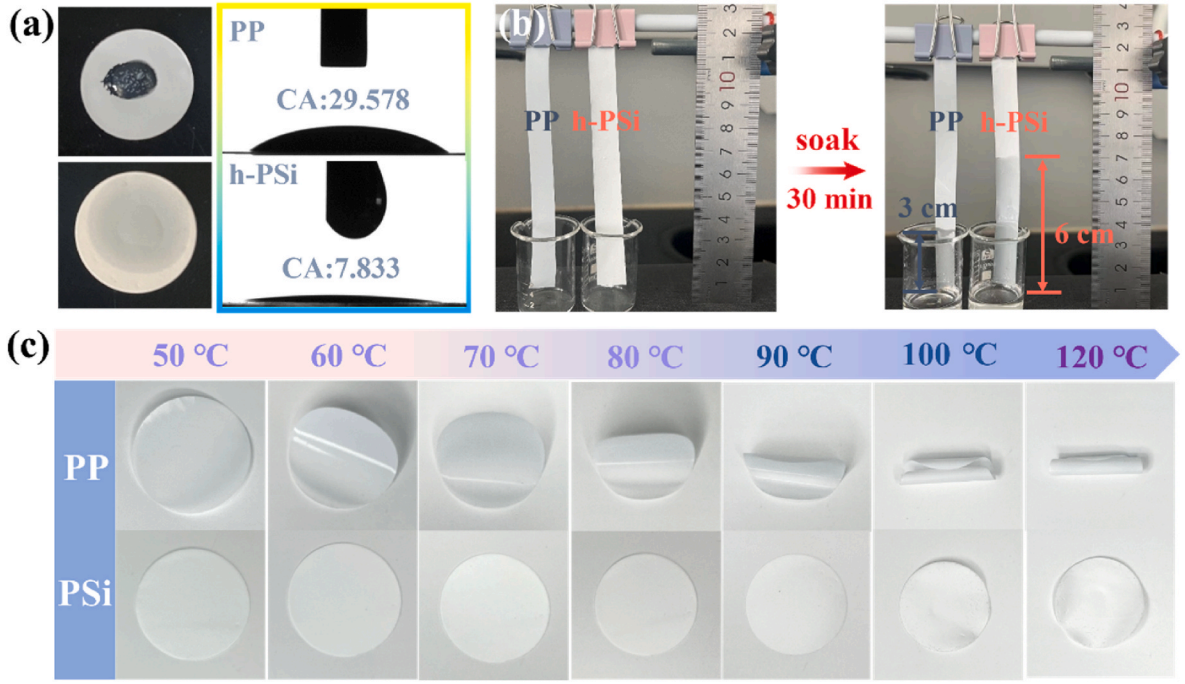

Fig. 2. (a) Contact angle tests between electrolyte and different membranes. (b) Electrolyte absorption tests and (c) heat resistance tests of different membranes.

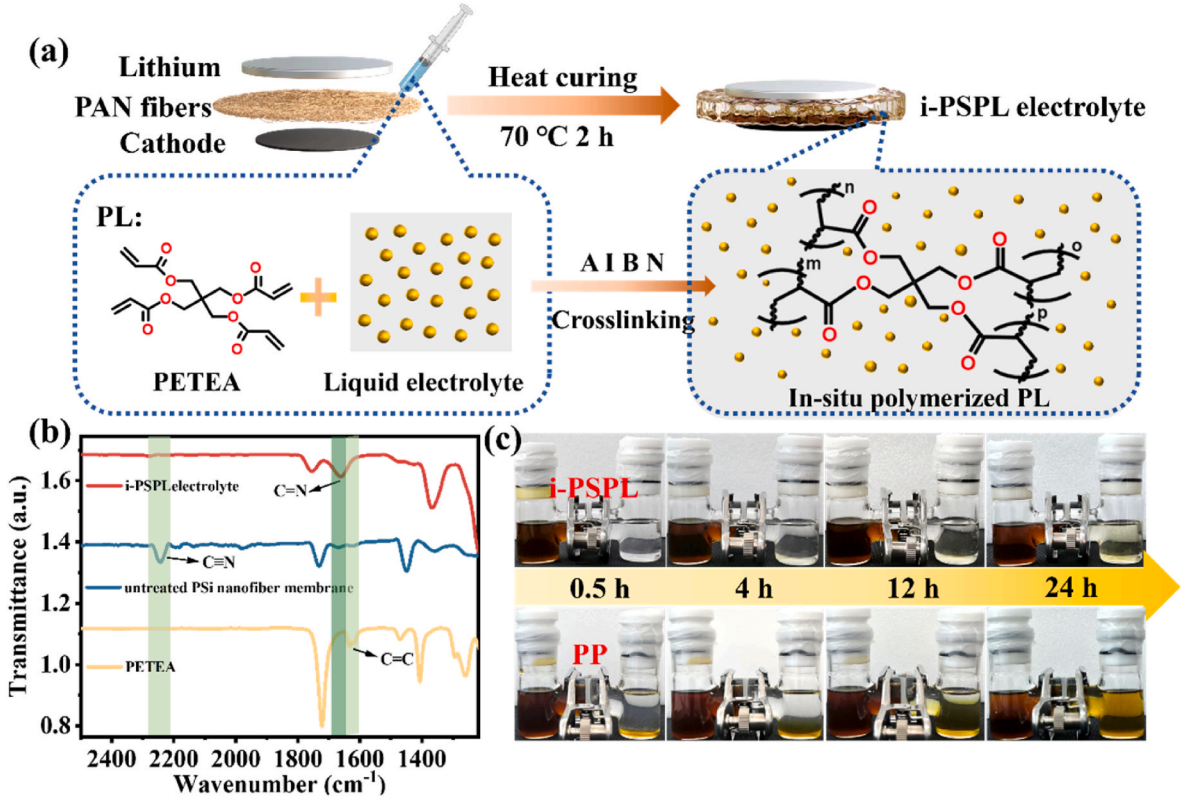

Fig. 3. (a) Synthesis scheme of PL and in-situ polymerized PL. (b) FTIR curves of PETEA, untreated PSi membrane, and i-PSPL after polymerization. (c) Polysulfide diffusion measurements of PP and i-PSPL membrane.

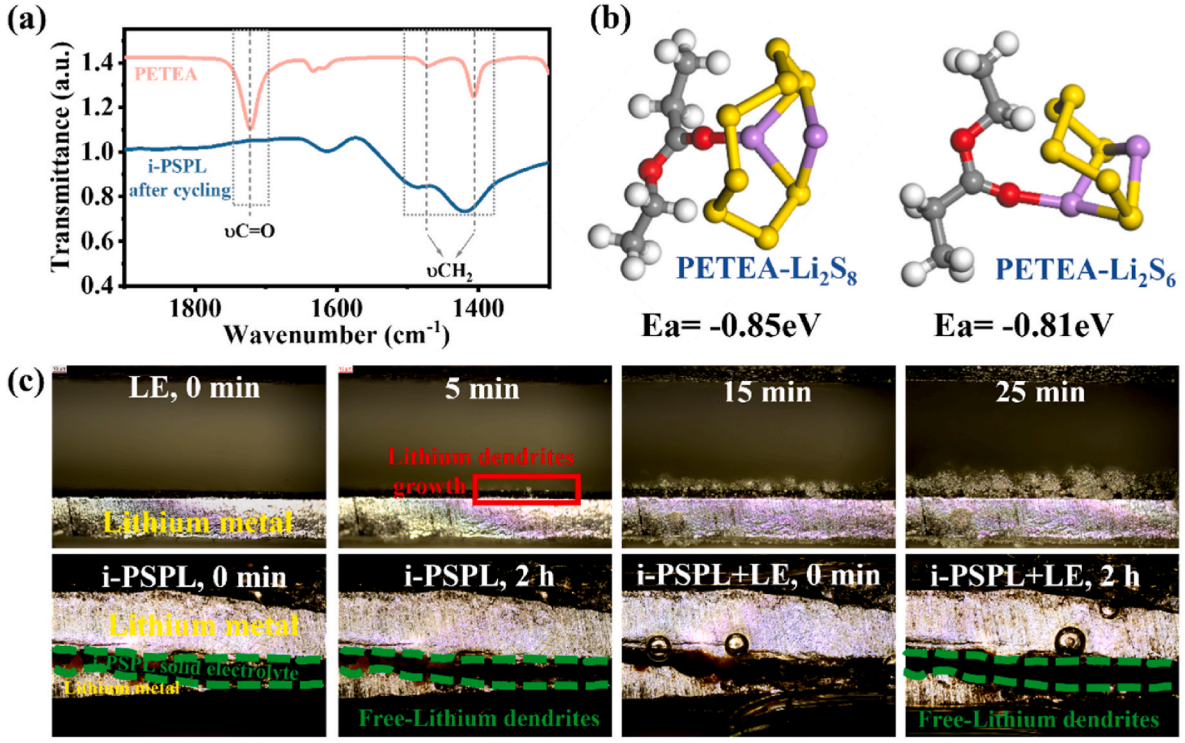

Fig. 4. (a) FTIR spectra of PETEA and i-PSPL after cycling. (b) The most stable adsorption cases between polysulfides (Li_2S_8 and Li_2S_6) and PETEA. (c) In-situ optical microscopy observation of lithium deposition using different electrolytes with increasing discharging time.

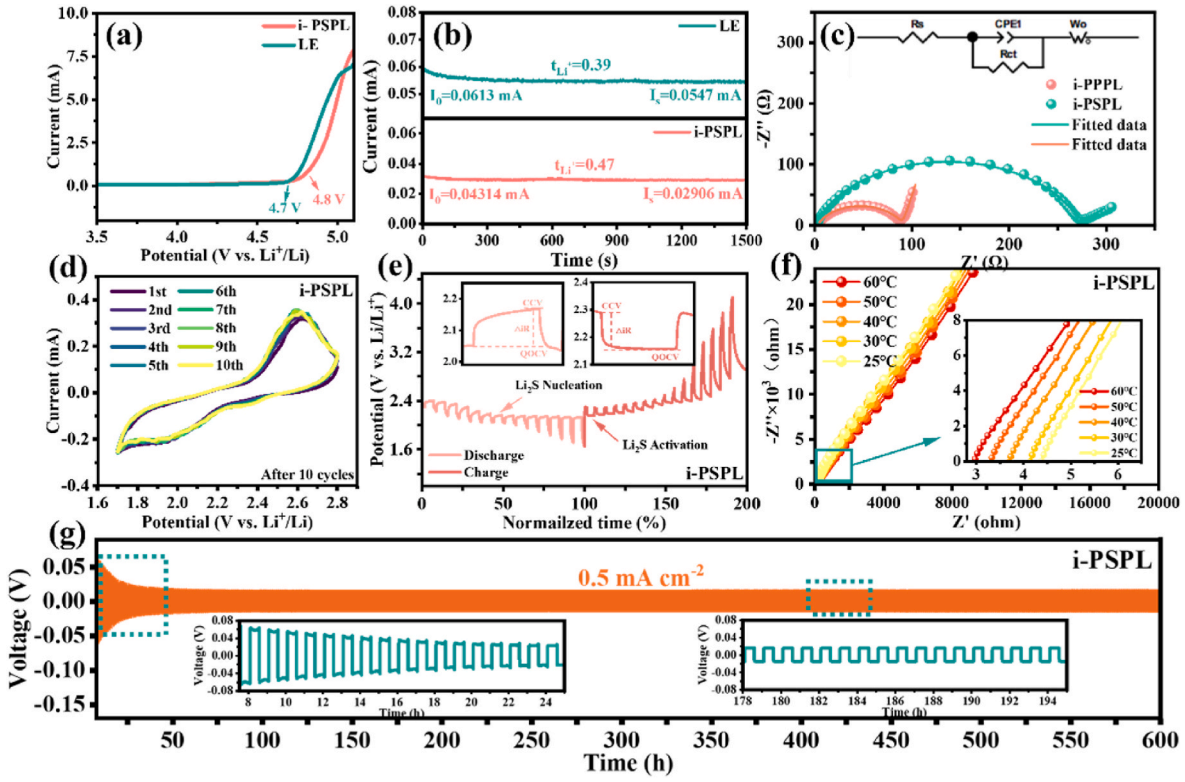

Fig. 5. (a) Electrochemical stability windows and (b) chronoamperometry curves of i-PSPL and LE. (c) EIS plots of 3D-SP/S||i-PPPL||Li and3D-SP/S||i-PSPL||Li. (d) CV curves after 10 cycles with i-PSPL. (e) GITT curve of battery with i-PSPL. (f) Nyquist plots and (g) long cycle test of symmetric cell at 0.5 mA cm^{-2} with i-PSPL.

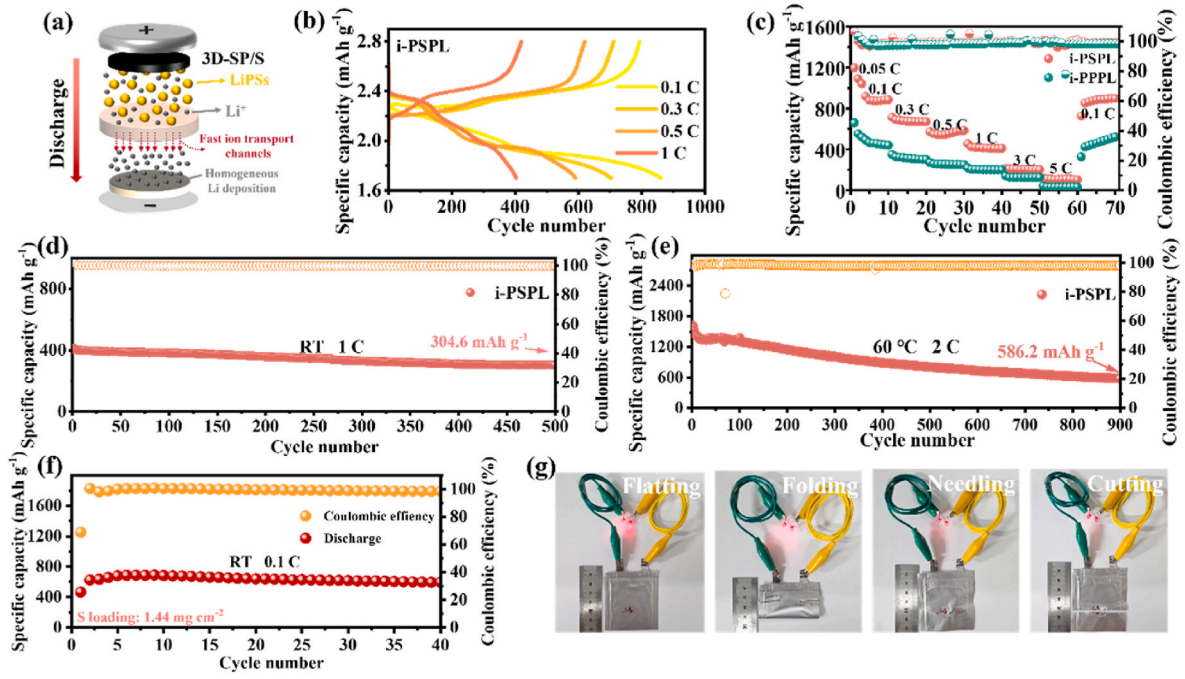

Fig. 6. (a) Illustration of Li^+ fast transport and uniform Li deposition. (b) Charge-discharge curves of 3D-SP/S||i-PSPL||Li battery at different rates. (c) Rate performances of 3D-SP/S||Li batteries employing i-PSPL and i-PPPL electrolytes at different current densities. Long-term cycling performance of 3D-SP/S||i-PSPL||Li battery at (d) 1 C, 25 °C and (e) 2 C, 60 °C. (f) Cycling stability of Li-S pouch cell with i-PSPL electrolyte. (g) Abusive tests of the pouch cell.

redox peaks of CV curves in Fig. 5d, further proving that the i-PSPL presents the characteristic of solid-state property. The rate performances with i-PSPL and i-PPPL electrolytes also were evaluated in Fig. 6c, we can observe that the battery with i-PSPL shows a higher reversible capacity between 0.05 C and 5 C, which are much higher than those of i-PPPL, indicating the superior electrochemical reversibility. The battery also delivers a specific capacity of 415.5 mAh g^{-1} at 1 C (Fig. 6d), and it still maintains a specific capacity of 304.6 mAh g^{-1} after 500 cycles, and

exhibits a minimal capacity decay of 0.052 % per cycle and a coulombic efficiency of 99.5 %. In contrast, the battery with i-PPPL electrolyte has a lower initial capacity and significant capacity decay at 1 C, with a specific capacity of only 122.36 mAh g^{-1} after 500 cycles (Fig. S19). In order to verify the i-PSPL electrolyte with excellent thermal stability, the electrochemical performance of i-PSPL was tested at a high temperature (60 °C). As shown in Fig. 6e, the i-PSPL battery shows an ultra-high discharge capacity of 586.2 mAh g^{-1} after 900 cycles even at 2 C, which fully demonstrated the electrochemical stability of the i-PSPL electrolyte. Cycling performances of the 3D-SP/S||i-PSPL||Li pouch cell at 0.1 C was shown in Fig. 6f, exhibiting stable cycle performance after 40 cycles. After treatment with extreme tests of folding, needling, and cutting, the pouch cell was still able to sustain a stable light output for LED, showing the reliability and stability of the battery under extreme environmental conditions (Fig. 6g).

3. Conclusion

In summary, an induced linkage mechanism realized by 3D electrode-electrolyte integration was proposed. 3D-SP provides space for LiPSs transport and PL, while SiO_2 in h-PSi and C=O functional group in polymerized PL can realize "adsorption-anchoring" of LiPSs, which makes i-PSPL a fast ion transport medium. The linkage conduction mechanism induced by polysulfides "adsorption-anchoring" process makes the batteries exhibit high room temperature ionic conductivity (7.34×10^{-3} S cm^{-1}) and ion mobility number (0.47). Therefore, the cells equipped with the 3D-SP/S cathode and i-PSPL electrolyte show a capacity decay of only 0.052 % per cycle at 1 C over 500 cycles, and achieving long-term cycling with low overpotential (145 mV) at 0.5 mA cm^{-2}. Even the pouch cell can endure stable cycling for 40 cycles at 0.1 C (25 °C), exhibiting commendable safety under extreme conditions. The mechanism provides novel insights into the design integrated solid-state electrolytes with excellent charge transfer kinetics and inhibition of shuttle effect in Li-S batteries.

CRediT authorship contribution statement

Hongxu Zhou: Writing – original draft, Resources, Data curation. **Yiyang Zhao:** Visualization, Investigation. **Xiaoning Wang:** Validation, Software. **Jingang Zheng:** Supervision, Project administration. **Weichen Han:** Formal analysis, Data curation. **Hongwei Zhao:** Methodology, Funding acquisition. **Han Zhang:** Investigation. **Lixiang Li:** Validation. **Xin Geng:** Project administration. **Baigang An:** Supervision, Funding acquisition. **Chengguo Sun:** Writing – review & editing, Funding acquisition.

Declaration of competing interest

The authors declare that they have no known competing financial interests or personal relationships that could have appeared to influence the work reported in this paper.

Acknowledgements

The authors gratefully acknowledge financial supported by the National Natural Science Foundation of China (11972178 and 52371224), the Nature Science Foundation of Liaoning Province (2023-BS-184). Distinguished Professor Project of Education Department of Liaoning and the Open Project Found of Key Laboratory of Energy Materials and Electrochemistry Liaoning Province are acknowledged.

Appendix A. Supplementary data

Supplementary data to this article can be found online at https://doi.org/10.1016/j.jpowsour.2025.238403.

Data availability

Data will be made available on request.

References

[1] B.B. Gicha, L.T. Tufa, N. Nwaji, X. Hu, J. Lee, Advances in all-solid-state lithium–sulfur batteries for commercialization, Nano-Micro Lett. 16 (2024) 172, https://doi.org/10.1007/s40820-024-01385-6.
[2] Y. Guo, P. Sireesha, C. Wang, L. Ren, C. Ying, J. Liu, W.-H. Zhong, An interpenetrated protein-polar polymer interlayer for suppressing shuttle effect in Li-S batteries, J. Power Sources 630 (2025) 236145, https://doi.org/10.1016/j.jpowsour.2024.236145.
[3] S. Grabe, M. Dent, T. Zhang, S. Tennison, C. Lekakou, A physicochemical model-based digital twin of Li–S batteries to elucidate the effects of cathode microstructure and evaluate different microstructures, J. Power Sources 580 (2023) 233470, https://doi.org/10.1016/j.jpowsour.2023.233470.
[4] L. Hu, T. Yang, L. Zhou, X. Yan, Y. Liu, Y. Xia, W. Zhang, J. Zhang, Y. Gan, X. He, X. Xia, R. Fang, X. Tao, H. Huang, In situ polymerization Bi-functional gel polymer electrolyte for high performance quasi-solid-state lithium−sulfur batteries, Small 20 (2024) 2402862, https://doi.org/10.1002/smll.202402862.
[5] C. Xian, Q. Wang, Y. Xia, F. Cao, S. Shen, Y. Zhang, M. Chen, Y. Zhong, J. Zhang, X. He, X. Xia, W. Zhang, J. Tu, Solid-state electrolytes in lithium–sulfur batteries: latest progresses and prospects, Small 19 (2023) 2208164, https://doi.org/10.1002/smll.202208164.
[6] F. Pei, L. Wu, Y. Zhang, Y. Liao, Q. Kang, Y. Han, H. Zhang, Y. Shen, H. Xu, Z. Li, Y. Huang, Interfacial self-healing polymer electrolytes for long-cycle solid-state lithium-sulfur batteries, Nat. Commun. 15 (2024) 351, https://doi.org/10.1038/s41467-023-43467-w.
[7] Y. Zhou, J. Ding, Z. Wei, W. Lei, J. You, Q. Zhang, D. Shi, The study on the reason why ZnS catalyst cannot suppress the shuttle effect of polysulfides in lithium-sulfur (Li–S) battery, J. Power Sources 615 (2024) 235084, https://doi.org/10.1016/j.jpowsour.2024.235084.
[8] D. Shao, L. Yang, K. Luo, M. Chen, P. Zeng, H. Liu, L. Liu, B. Chang, Z. Luo, X. Wang, Preparation and performances of the modified gel composite electrolyte for application of quasi-solid-state lithium sulfur battery, Chem. Eng. J. 389 (2020) 124300, https://doi.org/10.1016/j.cej.2020.124300.
[9] X. Judez, M. Martinez-Ibañez, A. Santiago, M. Armand, H. Zhang, C. Li, Quasi-solid-state electrolytes for lithium sulfur batteries: advances and perspectives, J. Power Sources 438 (2019) 226985, https://doi.org/10.1016/j.jpowsour.2019.226985.
[10] H.-N. Choi, H. Kim, M.-J. Kim, Y.-K. Sun, Constructing the interconnected charge transfer pathways in sulfur composite cathode for all-solid-state lithium–sulfur batteries, ACS Appl. Mater. 16 (2024) 11076–11083, https://doi.org/10.1021/acsami.3c18675.
[11] L. Bi, J. Xiao, Y. Song, T. Sun, M. Luo, Y. Wang, P. Dong, Y. Zhang, Y. Yao, J. Liao, S. Wang, S. Chou, Sulfhydryl-functionalized CoF-based electrolyte strengthens chemical affinity toward polysulfides in quasi-solid-state Li-S batteries, Carbon Energy 6 (2024) e544, https://doi.org/10.1002/cey2.544.
[12] Y. Xie, J. Ao, L. Zhang, Y. Shao, H. Zhang, S. Cheng, X. Wang, Multi-functional bilayer carbon structures with micrometer-level physical encapsulation as a flexible cathode host for high-performance lithium-sulfur batteries, Chem. Eng. J. 451 (2023) 139017, https://doi.org/10.1016/j.cej.2022.139017.
[13] Y. Xie, W. Zheng, J. Ao, Y. Shao, X. Huang, H. Li, S. Cheng, X. Wang, Multifunctional Ni-doped $CoSe_2$ nanoparticles decorated bilayer carbon structures for polysulfide conversion and dendrite-free lithium toward high-performance Li-S full cell, Energy Storage Mater. 62 (2023) 102925, https://doi.org/10.1016/j.ensm.2023.102925.
[14] Z. Chen, J. Wu, Y. Yang, L. Yan, X. Gao, Achieving a smooth "adsorption-diffusion-conversion" of polysulfides enabled by MnO_2-ZnS p-n heterojunction for Li-S battery, J. Colloid Interface Sci. 666 (2024) 322–330, https://doi.org/10.1016/j.jcis.2024.04.001.
[15] J. Li, G. Li, R. Wang, Q. He, W. Liu, C. Hu, H. Zhang, J. Hui, F. Huo, Boron-doped dinickel phosphide to enhance polysulfide conversion and suppress shuttling in lithium–sulfur batteries, ACS Nano 18 (2024) 17774–17785, https://doi.org/10.1021/acsnano.4c03315.
[16] S. Qiang, Z. Li, S. He, H. Zhou, Y. Zhang, X. Cao, A. Yuan, J. Zou, J. Wu, Y. Qiao, Modulating electronic structure of CoS_2 nanorods by Fe doping for efficient electrocatalytic overall water splitting, Nano Energy 134 (2025) 110564, https://doi.org/10.1016/j.nanoen.2024.110564.
[17] Y. Zhang, Z. Li, S. He, Y. Qiao, A. Yuan, J. Wu, H. Zhou, Interfacial engineering of heterostructured CoP/FeP nanoflakes as bifunctional electrocatalyts toward alkaline water splitting, J. Colloid Interface Sci. 679 (2025) 20–29, https://doi.org/10.1016/j.jcis.2024.10.084.
[18] S. Liao, Y. Xie, W. Zheng, Z. Huang, H. Zhang, Z.-Z. Luo, F. Zeng, C. Yang, S. Cheng, X. Wang, Enhancing rate performance in lithium-sulfur batteries via synergistic bidirectional catalysis and improved conductivity, Chem. Eng. J. 506 (2025) 160022, https://doi.org/10.1016/j.cej.2025.160022.
[19] A. Le Mong, J.C. Shin, M. Lee, D. Kim, Accelerated single li-ion transport in solid electrolytes for lithium–sulfur batteries: poly(arylene ether sulfone) grafted with pyrrolidinium-terminated poly(ethylene glycol), Small 20 (2023) 2309162, https://doi.org/10.1002/smll.202309162.

[20] S. Yanagihara, J. Huebner, Z. Huang, A. Inoishi, H. Akamatsu, K. Hayashi, S. Ohno, Compatibility of halide electrolytes in solid-state Li–S battery cathodes, Chem. Mater. 37 (2024) 109–118, https://doi.org/10.1021/acs.chemmater.4c02159.
[21] H. Park, A. Le Mong, D. Kim, Single and multilayer composite electrolytes for enhanced Li-ion conductivity with restricted polysulfide diffusion for lithium–sulfur battery, Mater. Today Energy 33 (2023) 101274, https://doi.org/10.1016/j.mtener.2023.101274.
[22] R. Deng, B. Ke, Y. Xie, S. Cheng, C. Zhang, H. Zhang, B. Lu, X. Wang, All-solid-state thin-film lithium-sulfur batteries, Nano-Micro Lett. 15 (2023) 73, https://doi.org/10.1007/s40820-023-01064-y.
[23] H. Zhou, W. Han, H. Chai, H. Huang, J. Zheng, H. Zhang, L. Li, W. Zhou, B. An, C. Sun, Metal-ion exsolution effect to accelerate the reaction kinetics in Li–S batteries, J. Mater. Chem. A. 12 (2024) 20238–20246, https://doi.org/10.1039/d4ta03248a.
[24] H. Li, D. Wu, J. Wu, L.Y. Dong, Y.J. Zhu, X. Hu, Flexible, high-wettability and fire-resistant separators based on hydroxyapatite nanowires for advanced lithium-ion batteries, Adv. Mater. 29 (2017) 1703548, https://doi.org/10.1002/adma.201703548.
[25] X. Li, K. Liu, N. Dong, B. Liu, G. Tian, S. Qi, D. Wu, A dendrite-blocking polyimide-meta-aramid separator with ultrahigh strength and thermostability for high-security lithium-ion battery, Chem. Eng. J. 481 (2024) 148525, https://doi.org/10.1016/j.cej.2024.148525.
[26] C. Xing, H. Chen, S. Qian, Z. Wu, A. Nizami, X. Li, S. Zhang, C. Lai, Regulating liquid and solid-state electrolytes for solid-phase conversion in Li–S batteries, Chem 8 (2022) 1201–1230, https://doi.org/10.1016/j.chempr.2022.01.002.
[27] J. Chen, Y. Zhuang, Y. Qiao, Y. Zhang, A. Yuan, H. Zhou, Co/Co_7Fe_3 heterostructures with controllable alloying degree on carbon spheres as bifunctional electrocatalyst for rechargeable zinc-air batteries, Int. J. Min. Met. Mater. 32 (2024) 476–487, https://doi.org/10.1007/s12613-024-2958-9.
[28] S. Wang, Y. Li, X. Zhou, Y. Yang, G. Chen, Lithiophilic SiO_2 nanoparticle pillared mxene nanosheets for stable and dendrite-free lithium metal anodes, J. Mater. Chem. A. 11 (2023) 20165–20173, https://doi.org/10.1039/d3ta03877g.
[29] T. Zhang, J. Zhang, S. Yang, Y. Li, R. Dong, J. Yuan, Y. Liu, Z. Wu, Y. Song, Y. Zhong, W. Xiang, Y. Chen, B. Zhong, X. Guo, Facile in situ chemical cross-linking gel polymer electrolyte, which confines the shuttle effect with high ionic conductivity and li-ion transference number for quasi-solid-state lithium–sulfur battery, ACS Appl. Mater. 13 (2021) 44497–44508, https://doi.org/10.1021/acsami.1c16148.
[30] M. Liu, H.R. Jiang, Y.X. Ren, D. Zhou, F.Y. Kang, T.S. Zhao, In-situ fabrication of a freestanding acrylate-based hierarchical electrolyte for lithium-sulfur batteries, Electrochim. Acta 213 (2016) 871–878, https://doi.org/10.1016/j.electacta.2016.08.015.
[31] D. Bosubabu, S. Ramakumar, S. Jeevanantham, I. Kanagaraj, P.B. Bhargav, N. Ahmed, K. Ramesha, In-situ lithiated SiO_2 as lithium-free anode for lithium-sulfur batteries, Batteries Supercaps 5 (2022), https://doi.org/10.1002/batt.202200262.